

Journal of Materials Chemistry C

Accepted Manuscript



This is an *Accepted Manuscript*, which has been through the Royal Society of Chemistry peer review process and has been accepted for publication.

Accepted Manuscripts are published online shortly after acceptance, before technical editing, formatting and proof reading. Using this free service, authors can make their results available to the community, in citable form, before we publish the edited article. We will replace this *Accepted Manuscript* with the edited and formatted *Advance Article* as soon as it is available.

You can find more information about *Accepted Manuscripts* in the [Information for Authors](#).

Please note that technical editing may introduce minor changes to the text and/or graphics, which may alter content. The journal's standard [Terms & Conditions](#) and the [Ethical guidelines](#) still apply. In no event shall the Royal Society of Chemistry be held responsible for any errors or omissions in this *Accepted Manuscript* or any consequences arising from the use of any information it contains.

Gravure Printed Sol-Gel Derived AlOOH Hybrid Nanocomposite Thin Films for Printed Electronics

Cite this: DOI: 10.1039/x0xx00000x

Received 00th January 2012,
Accepted 00th January 2012

DOI: 10.1039/x0xx00000x

www.rsc.org/

Terho Kololuoma^{a*}, Jaakko Leppäniemi^a, Himadri Majumdar^a, Rita Branquinho^b, Elena Herbei Valcu^c, Viorica Musat^c, Rodrigo Martins^b, Elvira Fortunato^b and Ari Alastalo^a

We report a sol-gel approach to fabricate aluminum-oxy-hydroxide (AlOOH) -based inks for gravure printing of high-dielectric-constant nanocomposite films. By reacting 3-glycidoxypropyl-trimethoxysilane (GPTS) with aluminum-oxide-hydroxide (AlOOH) nanoparticles under constant bead milling, inks suitable for gravure printing were obtained. The calculated relative dielectric constant based on measured capacitances and film thicknesses for the gravure-printed GPTS:AlOOH nanocomposite varied between 7 and 11 at a 10 kHz frequency. The dielectric constant depended on the mixing ratio of the composite and was found to follow the Maxwell-Garnett ternary-system mixing rule indicating presence of micro/nanopores that affect the electrical properties of the fabricated films. Increasing leakage current with increasing AlOOH content was observed. High leakage current was reduced by printing two-layer films. The double-layered gravure-coated films exhibited similar capacitance density but clearly lower leakage current and less electrical breakdowns in comparison to single-layered films having comparable film compositions and film thicknesses. The best composite yielded a capacitance density of 109 ± 2 pF/mm² at the 10 kHz frequency and a leakage current density of 60 ± 20 μ A/cm² at 0.5 MV/cm electric field as a single layer. The calculated relative dielectric constant at the 10 kHz frequency for this composition was 11.2 ± 0.5 .

Introduction

During the past years, the fabrication of electronic devices and circuits using roll-to-roll (R2R) printing methods has been under extensive study¹. Among these devices, printed layers of conductors, mainly based on nano silver inks, various semiconductors and dielectrics are combined for thin film transistors (TFTs)²⁻⁴, photovoltaic cells⁵, organic light emitting diodes⁶, radio frequency identification (RFID) tags for wireless communication^{3,7}, and digital and analogue circuits based on active and passive components². For these printed electronic devices, solution processable materials, known as inks, act as the main building blocks. For R2R-printing purposes, these inks need to be converted swiftly and at low processing temperatures to uniform and well defined layers with desired electrical properties.

Due to its vital role in electronics, the TFT is one of the most investigated printed electronic components. For printed and liquid phase processable TFTs, organic, inorganic and carbon

nanotube-based (CNT) semiconductors have been under intensive development^{3,8-10}. However for a TFT, the dielectric layer plays as important role as the semiconductor and during the past years, studies on solution processable organic, inorganic-organic hybrid and self-assembled monolayer dielectric layers have emerged^{11,12}. For a TFT with reasonably low operating voltages, the gate dielectric layer needs to be thin and have a relative dielectric constant ϵ_r as high as possible to achieve a sufficient gate capacitance. Moreover, the dielectric film should guarantee low leakage currents and also produce a smooth layer of uniform thickness upon printing. The printing process defines some additional requirements for the dielectric material, such as good film forming capability with high pattern definition and demand for the solvent system of the dielectric layer to be compatible with other layers in the device stack. In general, the ink used for the top layer, needs to wet the underlying film without the solvent system of the top layer dissolving the underlying layer.

Inorganic materials, such as metal oxides, provide a wide range of material choices having a high relative dielectric constant of $\epsilon_r > 9$ ¹². However, conventionally inorganic materials need to be deposited either by vacuum methods, such as sputtering and atomic layer deposition (ALD), or by anodization, which all provide an excellent film quality but are not optimal for printed electronics. Another commonly discussed drawback for inorganic materials is their brittleness which may reduce their suitability for flexible applications. Organic polymers, on the other hand, offer a material family with good processability but

^a VTT, Technical Research Centre of Finland, Kaitovayla 1, 90570 Oulu, Finland

^b CENIMAT/I3N Departamento de Ciência dos Materiais, Faculdade de Ciências e Tecnologia (FCT), Universidade Nova de Lisboa (UNL), and CEMOP/UNINOVA, 2829-516 Caparica, Portugal

^c Centre of Nanostructures and Functional Materials-CNMF, "Dunărea de Jos" University of Galati, 111 Domneasca, 800201, Galati, Romania

typically also much lower ϵ_r values¹², with some exceptions such as cyano resins providing ϵ_r value of around 18¹³.

For the solution processable and printable high ϵ_r dielectrics, methodologies to combine good material properties of both inorganic and organic materials are required. Therefore, hybrid material approaches where the good processability and flexibility of organic materials and high ϵ_r of oxide dielectrics are combined have been studied¹². From the R2R-printability point of view, the approach where the hybrid material is achieved by dispersing oxide nanoparticles in polymeric carrier offers a facile way to achieve a dielectric ink having rheological properties rather close to those of conventional inks used in R2R-printing. For TFT fabrication binary metal oxides such as TiO₂¹⁴⁻¹⁶ Ta₂O₅¹⁷ and Al₂O₃¹⁸ or ternary oxide such as BaTiO₃^{3,19,20} incorporated in various types of polymeric matrices have already been realized. Recently, some more complex oxides such as Ca₂Nb₃O₁₀ have been also utilized²¹. However, only a few of the previous reports have focused on up-scalable industrial printing processes³.

Fabrication of a printable inorganic-organic hybrid ink requires that a stable and well dispersed oxide suspension is obtained. Silane alkoxides with organic side chains are an interesting group of materials that can be used as gapping agents and dispersants for metal oxide nanoparticles²². In addition, organically modified silane alkoxides can also act as an inorganic-organic network-forming binder and therefore an additional polymer matrix may not be needed. Among these hybrid nanocomposites are aluminium oxide hydroxide (AIOOH) also known as Boehmite nanoparticles dispersed in 3-glycidyloxypropyl trimethoxysilane (GPTS) which acts both as the gapping agent and the network-forming precursor. Epoxy functionalized glycidyloxypropyl side chains are capable of forming a poly(ethylene oxide) network, catalysed by AIOOH nanoparticles, providing the required toughness and flexibility of printed dielectric films. This methodology was originally introduced by *Schmidt et al.* for the fabrication of abrasion resistant coatings on plastic²² and later by *J. Mauricio et al.*²³. *Noh et al.* have used a similar approach to enhance the dispersability of aluminum oxide (Al₂O₃) in poly(4-vinyl phenol) (PVP) polymer matrix for TFT applications¹³. In that work, with 24 vol.-% Al₂O₃ load the relative dielectric constant increased from 4.9 for pure PVP to 7.2 for the composite. In the literature, reported ϵ values for AIOOH are 1.5-2 times higher than that of aluminium oxide²⁴ which has been reported to have a dielectric constant of ~9-10^{25,26}.

In this paper we report on gravure-printed thin films with AIOOH:GPTS nanocomposite inks that provide dielectric films with high ϵ_r for printed electronic applications. Our results show unexpected ϵ_r values with increasing AIOOH content of the film. This can be due to the presence of air pores at high AIOOH loading ratios. The explanation is supported by porosity detected in BET-analysis (Brunauer, Emmett and Teller) and a theoretical fitting of the measurements to the Maxwell-Garnet mixing rules. Additionally, we find that a two-layered approach of film-formation increases performance and

reliability in comparison to their one layered counterparts in terms of leakage current and electrical breakdown.

Experimental section

Common methodologies, introduced by *Schmidt et al.*, to synthesize sol-gel-derived hybrid inorganic-organic nanocomposites have been applied for the fabrication of (3-glycidyloxypropyl) trimethoxysilane- (GPTS) functionalized AIOOH composite²². For the fabrication of inks, AIOOH powder (Condea P2, also available as Sasol dispersal P2) with average particle size of 25 nm, surface area of 260 m²/g and crystal size of 4.5 nm by manufacturer specification was used. AIOOH was selected for the experiments as it can be easily dispersed with reasonable amounts allowing the fabrication of high AIOOH load nanocomposites and as it was also readily available in large quantities. Condea P2 is actually a pseudoboehmite differing by Boehmite, however, only by its higher water content and by its higher surface area²⁷. According to manufacturer's specification Boehmite powder contains approximately 24 % of water. GPTS (Sigma-Aldrich) was used without further purification.

In a typical process, 2 g of AIOOH powder was weighted into a flask equipped with a magnetic stirring bar followed by the addition of 2-butoxy ethanol (Sigma-Aldrich), where the amount of 2-butoxy ethanol was half of the total amount used in an ink. The solution was stirred for 30 minutes and GPTS was then added drop by drop in to the suspension and let to stir for an hour. GPTS to AIOOH w/w ratios were varied from 1:2 to 4:1. Then 2 ml of 0.1 M HNO₃ was added to the solution and the solution was stirred for an additional hour. Then rest of the 2-butoxy ethanol and ZrO₂ beads (Sigmund-Lindner) having diameters between 200 μ m and 300 μ m were added into the solution. The amount of ZrO₂ beads was half of the total volume of the fabricated sol. To breakdown agglomerates and to allow formation of a homogenized ink, the sols were let to rotate in a roller bench for a week after which the solutions were filtered through a 1 μ m glass-fibre syringe filter. The compositions of fabricated inks are given in Table 1.

Rheology of the fabricated inks was determined using an Anton Paar MCR 301 Rheometer. The viscosity of the fabricated inks was measured as a function of the shear rate in order to tune the viscosities of the inks to obtain similar printability and comparable results. DSC and TGA analyses were performed to determine proper annealing conditions for the prepared materials as well as to identify the chemical reactions occurring during the drying and annealing. The analyses were carried out using Q20 DSC and Q5000 IR TGA equipment equipped with

Table 1. Composition of GPTS:AIOOH nanocomposite inks

GPTS (g)	AIOOH (g)	GPTS:AIOOH w/w	2-butoxy ethanol (ml)
1	2	1:2	18
2	2	1:1	14
2.5	2	1.25:1	13
4	2	2:1	10
6	2	3:1	9
8	2	4:1	8

Fourier transform infrared spectroscopic (FTIR) and mass-spectroscopic (MS) analysers (Thermal Analysis, US) in air atmosphere between 25 – 450 °C with a heating rate of 5 °C/min. For the DSC/TGA analyses, samples were prepared by drying sols at 110 °C and collecting the residue. To study the pore size of the obtained printed films, BET-analysis was performed with Accelerated Surface Area and Porosimetry System ASAP2010 from Micromeritics. The crystallinity of the powder samples has been determined using a PANalytical's X'Pert PRO MRD X-ray diffractometer, with a monochromatic CuK α radiation source (wavelength 1.540598 Å). XRD measurements at room temperature have been carried out from 7° to 90° (2 θ), with a scanning step size of 0.05°.

Gravure printing experiments were performed using a Schläfli Labratester table-top printability tester equipped with a vibration engraved printing plate having eight patterned areas with different cell parameters. The cell shape was pyramidal. Ink transferring capacities and line densities were between 3.5 ml/m² and 12.2 ml/m², and 240 l/cm and 70 l/cm, respectively. The open area ratios were varied between 0.77 and 0.58 with the smallest being for the highest line density areas. The stylus and screen angles for all areas are equal being 120° and 45°, respectively. Width to length ratio of the cells decreased linearly from 2.1 to 1 with the increasing screen line densities. Single- and double-layer prints were made on molybdenum-coated 50 μ m thick poly(imide) (Mo-PI) substrates after which the samples were dried at 220 °C for 10 minutes. For the preparation of double layered samples, ink having the GPTS:AIOOH ratio of 2:1 was used. Patterns, printed with areas with ink transfer volumes of 10.4 ml/m² (cell raster 80 lines/cm, cell depth of 36 μ m) and 5.3 ml/m² (cell raster 140 lines/cm, cell depth of 21 μ m) were selected for the electrical characterisation. This selection was performed, because a double layer films printed with 140 l/cm areas yields the same thickness as a single layered film produced with 80 l/cm area. Hence, comparable film thicknesses between one and two layered samples can be achieved. Between each layer deposition, the samples were dried as described earlier.

The surface morphology was investigated by atomic force microscopy (AFM, Asylum MFP3D) and scanning electron microscopy (SEM-FIB, Zeiss Auriga Crossbeam microscope). For cross-section microscopy of the produced films and devices, cutting of the samples was performed by focused ion beam (FIB). In FIB milling experiments, Ga⁺ ions were accelerated to 30 kV at 100 pA and the etching depth was around 4 μ m. A sacrificial carbon layer of 50 nm was deposited to protect the samples. The film thicknesses were measured

using a stylus profilometer (DekTak 150) over an etched step which was formed by 1-5 min etching in 10 % KOH in H₂O at 50 °C. An ultraviolet (UV) light releasable adhesive was used as an etch resist.

For the electrical characterization of the gravure printed samples, metal-insulator-metal (MIM) capacitor structures were used with a common Mo bottom electrode and Au top electrodes of 400 μ m \times 400 μ m in size that were vacuum evaporated through a mask. Capacitances of the MIM capacitors were measured as a function of frequency ($C-f$) using a semiconductor analyser (Keithley 4200 SCS Keithley) with a parallel C_p-G_p - model at a frequency range of 1 kHz – 1 MHz. All the capacitance values reported in this paper are given at the frequency of 10 kHz. The capacitance and the AC conductance as a function of DC bias voltage ($C-V$) were measured from -10 V to +10 V at 10 kHz. The DC current voltage ($I-V$) curves of the MIM capacitors were measured using a source meter (Keithley 2636) and the leakage current density was determined at an electric field of 0.5 MV/cm. The minimum DC breakdown voltage was estimated from the $I-V$ measurements that were performed up to 1 MV/cm electric fields.

Results and discussion

DSC, TGA and XRD measurements

DSC and TGA measurements were performed to study the effect of the annealing temperature on the composition and stability of the GPTS:AIOOH films. The limiting factor for the annealing temperature is the onset of the decomposition of the epoxy chain in the GPTS precursor leading to a residual carbon crust in the film and hence increasing the leakage current. A set of five samples was analysed: pure AIOOH, hydrolysed and dried GPTS, which was synthesized according to the described process but without AIOOH, and from the fabricated series of GPTS:AIOOH nanocomposites three samples with different ratios of 1:2, 1:1 and 2:1.

In the DSC/TGA curves of pure AIOOH, shown in Fig. 1a) in black, three set of reactions can be seen. According to *Alphonse et al.*²⁸, the first endothermic reaction, between 100 °C and 150 °C has been attributed to desorption of physically absorbed water. The second exothermic reaction without a mass loss at around 200 °C, marked with an asterisk, is related to transition of AIOOH to γ -alumina. The corresponding 15 % mass loss due to the transition of AIOOH to Al₂O₃ is not observed. This can be explained with the help of the observation made by *Alphonse et al.*²⁸ who noticed that the transition of AIOOH to alumina is a complex process involving four consecutive stages starting with desorption of first physisorbed and then chemisorbed water. The last stage after conversion to γ -alumina, between 200 °C and 450 °C, is the dehydration of γ -alumina which can be seen as a weak endothermic reaction with a corresponding and expected 15 % mass loss. In the corresponding DSC/TGA curves of pure GPTS, shown in Fig. 1a) in red, practically two steps of decomposition can be observed: a broad exothermic reaction

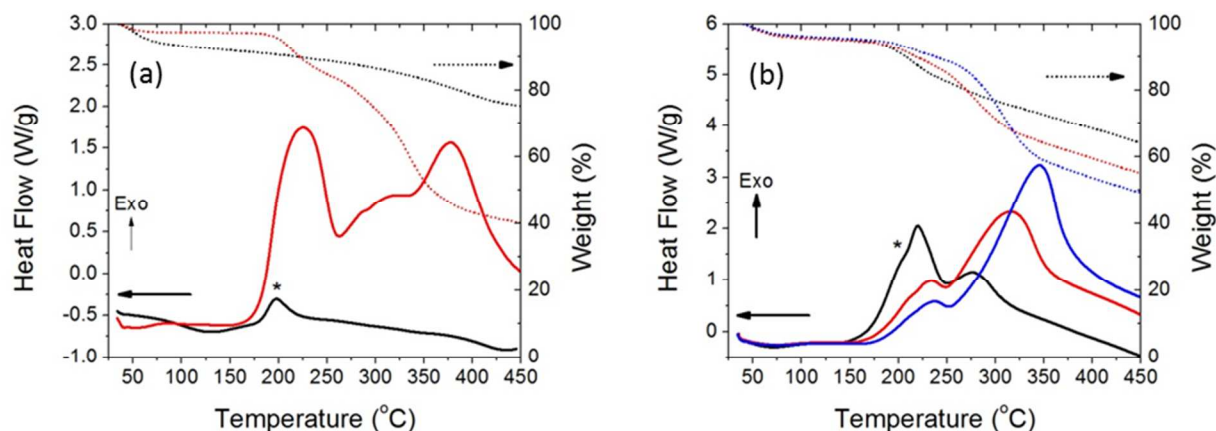


Fig. 1. a) DSC/TGA curves of AIOOH powder (black) and hydrolysed and dried GPTS (red). b) DSC/TGA-curves from samples having GPTS:AIOOH ratios of 1:2 (black), 1:1 (red), and 2:1 (blue). DSC-curves are indicated with solid lines whereas the TGA-curves are dotted. Asterisk (*) indicates the proposed temperature for AIOOH conversion to γ -alumina.

with corresponding mass loss at around 220 °C and a very broad exothermic reaction between 260 °C and 400 °C with a corresponding mass loss. The lower temperature decompositions can be assumed to be related to condensation reactions and hence to the elimination of water, hydroxyl and unreacted alkoxy groups while the higher temperature reactions can be assumed to result from the decomposition of glycidylxypropyl side chain in GPTS, respectively. Mass spectroscopy studies of decomposition products support this conclusion indicating that the first set of exothermic reactions at around 200 °C produces mainly water and some organic compounds, namely CH_2CH and CH_3CH_2 , and the second set of decomposition reactions at higher temperatures produces also more complex organic species.

DSC/TGA curves of GPTS:AIOOH nanocomposites, see Fig. 1b), highlight significant differences depending on the ratio of the two components, both around 200 °C and in the approximate range of 300–400 °C. In the case of GPTS:AIOOH 1:2 sample, two overlapping peaks with corresponding mass loss are observed around 200 °C. Based on the previous discussion it can be considered that the elimination of the water, OH groups and unhydrolysed alkoxide groups of GPTS is the major origin of this set of reactions. It can be assumed that transformation of AIOOH to γ -alumina also occurs at that temperature range, indicated by the asterisk, but according to the transformation peak integral, see Fig. 1a), this transformation can be assumed to have only a minor contribution to the overall reaction seen. With the increasing GPTS ratio the intensity of the peak at around 200 °C decreases. This can be assumed to be related to the decreasing number of free OH groups by condensation reactions between the GPTS molecules and/or between GPTS and AIOOH nanoparticles. However, in comparison to the reaction integral of pure GPTS, see Fig. 1a), these reactions are much less intense. Obviously, AIOOH is facilitating these condensation reactions which have likely occurred during the sample preparation phase when inks are

heated up to 110 °C. Such a difference may be also attributed to Lewis acid activity of Al-OH group on the hydrolysis of silicon alkoxides as shown earlier by Schmidt *et al.*²²

Another set of broad exothermic reactions at around 300 °C are shifting to clearly higher temperatures with higher GPTS load. Higher percentual mass loss was expected as increased amount of GPTS contains higher amount of decomposable glycidylxypropyl side chains. The gradual shifting of the exothermic reaction of nanocomposites with increasing GPTS content can be explained by the formation of more closed, e.g. less porous, film with increased GPTS amount. AFM studies which are reported later on this paper support this explanation. The DSC/TGA measurements reveal that the nanocomposite materials undergo some structural transitions as well as elimination of water and some organics starting at around 200 °C. These reactions likely result in nanocomposites with different amount of residual -OH and water which may induce some differences in the dielectric properties of the printed films. However, decomposition of organic side chains and/or network can be concluded to start at around 250 °C. This observation explains our earlier findings with the same type of materials obtained with different synthetic routes. Namely, we observed that leakage current is approximately 100 times higher for nanocomposites annealed at 250 °C as compared to those annealed at 200 °C²⁹.

XRD measurements of the Boehmite powder and synthesized nanocomposite with GPTS:AIOOH ratio of 1:1 were performed to follow the crystalline phases in the fabricated nanocomposites (Fig.2) Both samples show almost identical diffractograms corresponding to orthorhombic Boehmite phase (ICDD No. 98-009-2910). The only noticeable difference is a broad peak near 2θ 20°. According to J. Mauricio *et al.* the broad peak corresponds to siloxane counterpart²³ indicating the

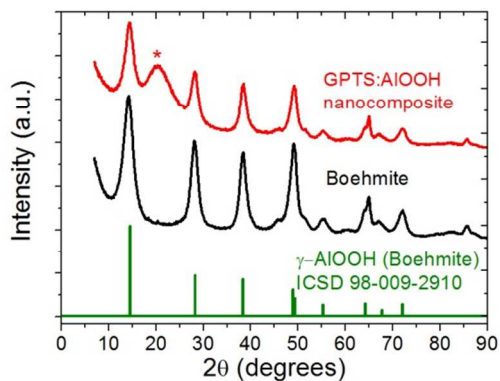


Fig. 2. Measured powder X-ray diffractograms for Boehmite powder (Condea P2), for the nanocomposite having the GPTS:AIOOH ratio of 1:1, and the diffractogram, major reflections, for γ -AIOOH (Boehmite) according to ICSD 98-009-2910. The asterisk indicates the additional siloxane phase.

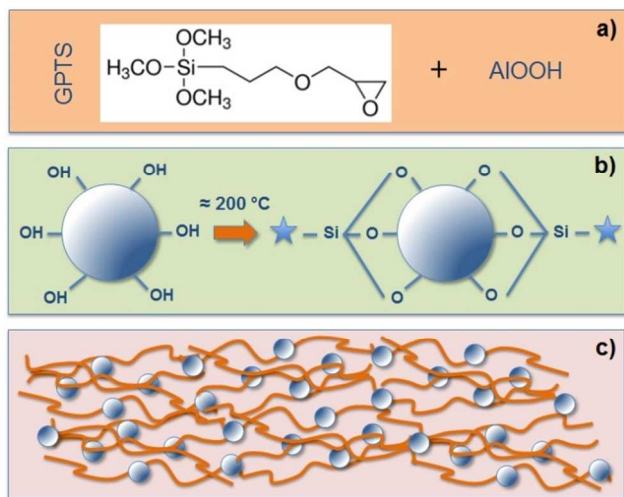


Fig. 3. Schematics of the hybrid nanocomposite formation. a) Chemical formulas for both compounds; b) Alkoxide condensation hydrolysis and condensation reactions lead to formation of inorganic network. Ring opening of glycidyloxypropyl side introduces organic network into a nanocomposite; c) Hybrid nanocomposite dielectric film formation through nanoparticle mediated polymer network.

presence of separate amorphous phase originating from the GPTS.

According to the DSC, TGA and XRD analysis we can conclude that the formation of GPTS:AIOOH nanocomposite was achieved. In Fig. 3 a schematic representation of the hybrid nanocomposites formation are shown.

Ink Characteristics and Printability

During the ink fabrication it was noticed that the viscosity of the fabricated inks increased with increasing GPTS content. Therefore, the amount of 2-butoxy ethanol was adjusted in order to obtain similar viscosities and hence printability between the inks with different GPTS:AIOOH w/w ratios, as shown in Table 1.

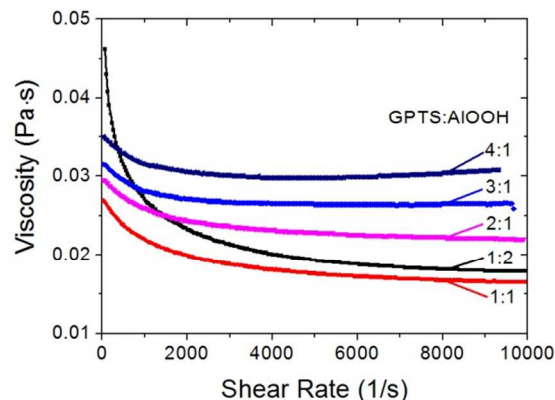


Fig. 4. Viscosities of the GPTS:AIOOH nanocomposite inks as a function of the shear rate.

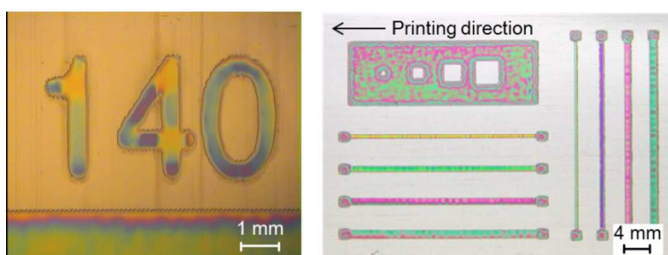


Fig. 5. Example from smooth and uniform gravure printed GPTS:AIOOH nanocomposite structures on Mo-PI. Patterns were printed using ink having GPTS:AIOOH w/w ratio of 2:1. Left: printed pattern having height of 3 mm and nominal width of 500 μm . Right: picture from the middle of the printed area.

In Fig. 4, the measured viscosities as a function of the shear rate are shown. As can be seen, viscosities of the fabricated inks are approximately in the same magnitude being between 0.015 and 0.035 Pa·s at the shear rate of 10000 s^{-1} . A clear pseudoplastic (shear thinning) behaviour of the ink is observed with the sample having the GPTS:AIOOH ratio of 1:2. However, pseudoplastic behaviour is clearly reduced for increasing GPTS content. This might result from the decreased particle-particle interaction due to the more complete AIOOH surface gapping by GPTS leading to an increased repulsive inter-particle potential and resulting hence in nearly shear-rate-independent viscosities³⁰, e.g. Newtonian behaviour, while the attractive particle networks exhibit shear-thinning behaviour as seen for the lower GPTS contents.

All fabricated GPTS:AIOOH inks yield a good printing quality and smooth, uniform layers were successfully printed on PET and on Mo-PI as shown in Fig. 5. As can be seen good line and pattern definition both parallel and perpendicular to the printing direction can be obtained. Also, uniform large area coverage without viscous fingering and without ink squeezing to the leaving edge can be seen. According to visual inspection the quality of the prints produced with different cell parameters are comparable. Film thicknesses are dependent upon engraving parameters.

Dielectric properties

The measured capacitance density, film thickness, leakage current and calculated dielectric constant at 10 kHz for the gravure printed films with varied GPTS:AIOOH w/w ratio are shown in Table 2. As expected, by increasing the amount of 2-butoxy ethanol (see Table 1) used to reduce the viscosities of the inks with lower GPTS contents, thinner films are obtained. On the other hand, it can be seen that the higher amount of added 2-butoxy ethanol, i.e. inks with lower amount of GPTS, results in lower variation of film thicknesses.

According to the obtained results, the capacitance density in the GPTS:AIOOH samples seems to first increase and then decrease with increasing GPTS content. Correspondingly, calculated ϵ_r values indicate a similar trend, which is not expected according to the binary mixing-rules of Lichtenecker³¹ and Maxwell-Garnet³², which expect the dielectric constant to increase as the amount of higher ϵ_r material in the film increases, a result that is also reported for other type of nanocomposites³³.

To illustrate the deviation of the obtained dielectric constants from the aforementioned mixing rules, we applied the Maxwell-Garnet mixing rule for calculating the effective dielectric constant of a binary composite, as shown in Equation 1. The effective dielectric constant for a binary composite is³²

$$\epsilon_{eff} = \epsilon_e + 3f\epsilon_e \frac{\epsilon_i - \epsilon_e}{\epsilon_i + 2\epsilon_e - f(\epsilon_i - \epsilon_e)} \quad (1)$$

where f denotes the fraction of the total volume occupied by the inclusions (dielectric spheres), ϵ_i the dielectric constant of the inclusions (spherical dielectric AIOOH nanoparticles) and ϵ_e the dielectric constant of the environment (GPTS matrix).

The volume fraction f was written as a function of GPTS:AIOOH weight ratio, $r = m_e/m_i$, as shown in Appendix (equation A1). The dielectric constant for GPTS, $\epsilon_e = 6$, was determined from a capacitor film fabricated from an ink where no AIOOH was added and for AIOOH nanoparticles, dielectric constant $\epsilon_i = 30$ was used. For the densities of AIOOH, we used

the value of 2.3 g/cm³ as measured by *Alphonse et al.*²⁸ and for GPTS, we estimated a density of 2.0 g/cm³ by assuming 90% conversion from GPTS to -O-Si-O- network.

As both densities and dielectric constants depend strongly on the amount of residual -OH and water, crystal water content of the AIOOH, and especially in the case of GPTS on the condensation rate of the alkoxide precursors as already discussed, some error probably exists in proposed numbers. However, regardless of the presumed values of density and dielectric constant for the components, the observed lowering of the dielectric constant towards higher AIOOH contents cannot be explained with a simple binary composite.

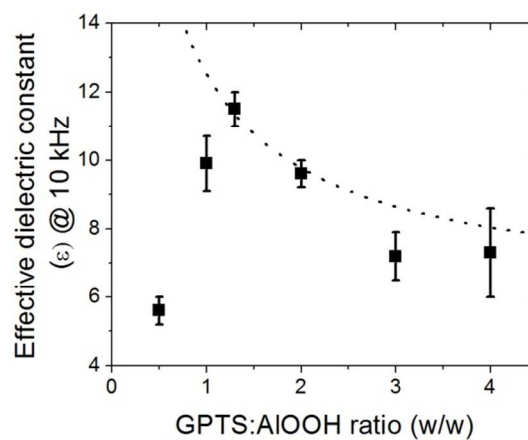


Fig. 6. The measured and calculated (square symbols with error bars) dielectric constant (ϵ_{eff}) of the GPTS:AIOOH films at 10 kHz as a function of increasing GPTS content. The calculated dielectric constant according to the Maxwell-Garnet two-component mixing rule is shown as a dashed line.

Table 2. Measured capacitances, film thicknesses, leakage currents and calculated dielectric constants at 10 kHz for gravure printed GPTS:AIOOH films. The results are shown for 9 capacitors of $\sim 400\mu\text{m} \times 400\mu\text{m}$ in size as the average value and the standard deviation except for thickness where the thickness is measured at three locations near the measured capacitors from which the average value and max-min error are calculated.

GPTS:AIOOH w/w	$r = m_{GPTS}/m_{AIOOH}$	C_p/A (pF/mm ²)	Thickness (nm)	I_{leak}/A @ 0.5 MV/cm ($\mu\text{A}/\text{cm}^2$)	ϵ @ 10 kHz
1:2	0.5	76.3 ± 1.4	650 ± 40	20 ± 3	5.6 ± 0.4
1:1	1.0	120 ± 3	730 ± 50	110 ± 20	9.9 ± 0.8
2.5:2	1.25	109 ± 2	910 ± 30	60 ± 20	11.2 ± 0.5
2:1	2.0	61.4 ± 1.1	1380 ± 40	2.1 ± 0.6	9.6 ± 0.4
3:1	3.0	46.7 ± 0.3	1360 ± 130	1.6 ± 0.4	7.2 ± 0.7
4:1	4.0	48 ± 3	1340 ± 230	1.1 ± 1.1	7.3 ± 1.4

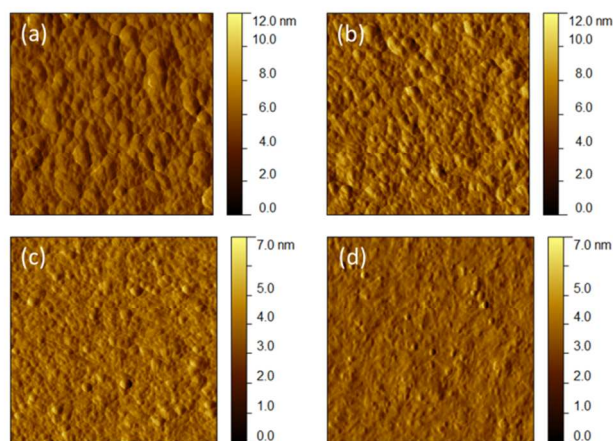


Fig. 7. AFM deflection images of samples with GPTS:AIOOH ratio of a) 1:2 b) 1:1 c) 2:1 and d) 4:1. Measured area is $1 \mu\text{m} \times 1 \mu\text{m}$ for all samples.

The most probable cause for this anomaly arises from the complex sol-gel chemistry. As it is well known, sol-gel processing results typically in a rather porous film due to the escaping water and alcohols during the gel conversion into a solid film³⁴. Therefore, it can be assumed that in a porous structure not only the hybrid silane resulting from the GPTS precursor and the AIOOH particles but also air in the pores of the fabricated film affect the effective dielectric constant. Therefore, to study the effective dielectric constant of the proposed ternary system, the Maxwell-Garnett mixing rule for ternary mixture was applied³²:

$$\epsilon_{eff} = \epsilon_e + 3\epsilon_e \frac{f_i \frac{\epsilon_i - \epsilon_e}{\epsilon_i + 2\epsilon_e} + f_{air} \frac{\epsilon_{air} - \epsilon_e}{\epsilon_{air} + 2\epsilon_e}}{1 - \left(f_i \frac{\epsilon_i - \epsilon_e}{\epsilon_i + 2\epsilon_e} + f_{air} \frac{\epsilon_{air} - \epsilon_e}{\epsilon_{air} + 2\epsilon_e} \right)}, \quad (2)$$

where f_i denotes the fraction of the total volume occupied by the inclusions (spherical dielectric AIOOH nanoparticles), f_{air} is the fraction of the total volume occupied by air (spherical voids) and ϵ_{air} the dielectric constant of air (≈ 1). In order to estimate the fraction of the pores, AFM measurements were applied to investigate the surface morphology of the films. AFM measurements of the films with GPTS:AIOOH ratios between 1:2 and 4:1 are shown in¹⁸.

From the AFM scans, see Fig. 7, one may conclude that with the increasing GPTS content the surface seems to be more compact. In addition, according to visual estimation of the samples having the GPTS:AIOOH ratios of 1:2 and 2:1, it can be concluded that some decrease in particle size from 65 nm to 45 nm, respectively, occurs. This observation indicates some level of aggregation with lower GPTS:AIOOH ratios.

The average roughness R_a and maximum roughness R_{max} from $1 \mu\text{m} \times 1 \mu\text{m}$ and $10 \mu\text{m} \times 10 \mu\text{m}$ areas together with the projected surface area increase of the films are shown in Fig. 8. According to the data, both R_a and R_{max} increase with increasing AIOOH content and the observed values clearly

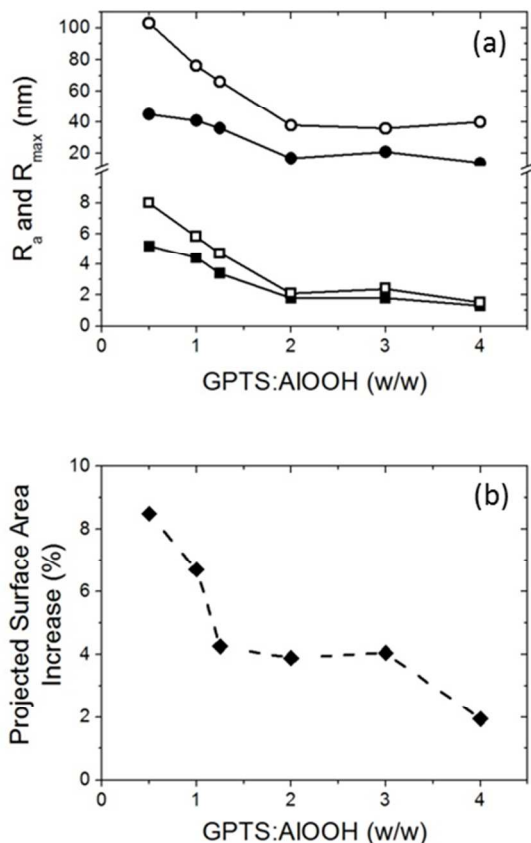


Fig. 8.a) Surface roughness's according to AFM measurements taken from $1 \mu\text{m} \times 1 \mu\text{m}$ area (filled symbols) and from $10 \mu\text{m} \times 10 \mu\text{m}$ areas (hollow symbols). Squares indicate R_a values and circles R_{max} values. b) Projected surface area increase ($1 \mu\text{m} \times 1 \mu\text{m}$).

indicate that the surface is more compact with increased GPTS amount. The measured R_a roughness with low AIOOH load is approximately at the same level as reported by *Noh et al.*¹⁸ who fabricated films using GPTS dispersed Al_2O_3 , doped in poly(vinyl phenol) matrix. On the other hand, *Kim et al.*²⁵ have obtained R_{max} and R_{rms} values in the range of 4 nm and 0.2 nm, respectively, by using ionic precursors. Therefore, it can be said that the physical size and shape of nanoparticles have a clear increasing effect to the porosity of dielectric film, especially when high solid loads are used. From the AFM data it can be also concluded that the percentual difference between the scan area and the projected surface area increases from around 1 % to over 8 % which possibly indicates an increase in the porosity and air volume in the films.

In order to get an estimation of the air volume, we also applied BET measurements to determine values for the pores volume. However, the method was only successful in the measurement of the sample with the highest GPTS:AIOOH ratio of 1:2 ($r = 0.5$) for which the pore volume of $0.33 \text{ cm}^3/\text{g}$ and average pore size of $\sim 5 \text{ nm}$ were obtained, as shown in Fig. 9.

The obtained values of BET surface area and pore volume are close to manufacturer specifications, as given in experimental section, which can indicate that the particles are only partly

covered by GPTS. With the help of the calculus shown in Appendix, we estimated the volume fraction of air f_{air} to be 0.42, indicating a clear deviation from the binary composite model for the sample with the lowest GPTS content. Based on the linearly decreasing projected surface area with increasing GPTS:AIOOH ratio shown in Fig. 8, we have estimated the pore volume V_{air} also as linearly decreasing for $0.5 \leq r \leq 1.1$ with values shown in Appendix Table A1 and as $V_{\text{air}} = 0$ for films with higher GPTS content ($r > 1.1$).

By using the calculated volume fraction of inclusions f_i and air f_{air} which are shown in Appendix Table A1, we can utilize the ternary mixing rule of equation (2) to take account the presence of air in the pores. The ternary model results in a peaking dielectric constant and a qualitatively agreeing fit within the set of dielectric constants for AIOOH $\epsilon_i = 20, 30$ and 40 , see Fig. 11. The dielectric constant yielding roughly the best fit with GPTS:AIOOH ratio in the range of $1 \leq r \leq 2$ is $\epsilon_i = 30$, which is clearly higher than earlier reported for AIOOH, whereas $\epsilon_i = 20$ results in a better fit outside the intermediate r range and is closer to the values reported earlier for AIOOH²⁴.

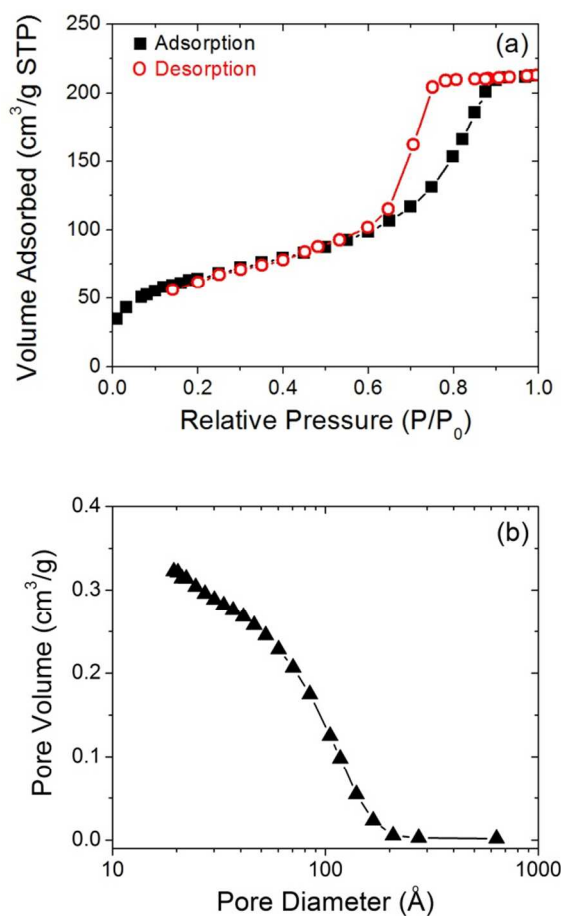


Fig. 9. a) Physisorption isotherms, black square correspond to gas adsorption and hollow red circles to gas desorption, and b) pore size distribution and cumulative pore volume for sample with GPTS:AIOOH ratio of 1:2.

The higher ϵ_i for the intermediate r range can possibly arise from H₂O ($\epsilon_{\text{H}_2\text{O}} = 80$) trapped in the film or on the AIOOH particles²⁸ after any condensation process taking place in the film and, thus, lead to an increase in the dielectric constant of the inclusions or the matrix. However, the detection of such a complex system is beyond the scope of this work. As a conclusion, the Maxwell-Garnett ternary mixing rule can on a general level explain the observed decreasing dielectric constant with high AIOOH and low GPTS loads.

I - V measurements reveal that the printed samples have breakdown fields above 1 MV/cm. However, as indicated in Table 2, leakage current is increasing with increasing AIOOH content in the film. Concurrently, the amount of shorted devices also increases, which supports the already observed phenomenon that a higher GPTS amount results in more efficient filling of the pores between the AIOOH particles and thus yields a less porous structure and less pinholes.

Fig. 10 summarizes the measured capacitance and dissipation factor as a function of frequency for sample having a GPTS:AIOOH ratio of 2:1. The measured capacitance as a function of DC bias voltage is also shown. In general, the samples with different ratios show characteristics, where the C - f shows slightly decreasing capacitance and the dissipation

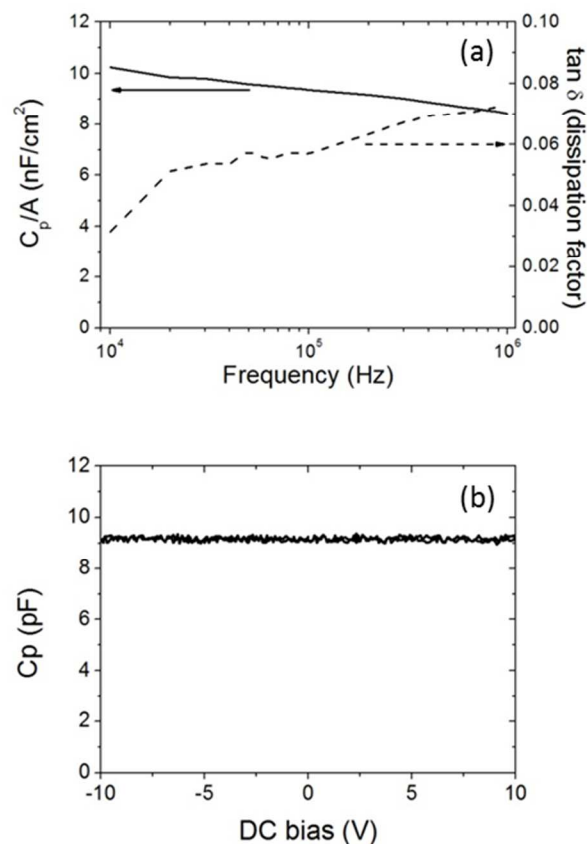


Fig. 10. Electrical properties of sample having GPTS:AIOOH ratio of 2:1. a) Measured capacitance (solid line) and dissipation factor (dashed line) as a function of frequency. b) Measured capacitance as a function of DC bias voltage at 10 kHz.

factor increases with increasing frequency. The capacitance density at 10 kHz roughly equals the capacitance density of 300 nm thick SiO₂, which is commonly used as a dielectric layer on Si-wafers. The C - V shows a flat capacitance with no hysteresis during the back and forth sweeps.

Double layered samples

To improve the applicability of the dielectric nanocomposite films for applications in printed electronic devices, it is essential to decrease the leakage current and to limit the occurrence of breakdowns, while preserving the capacitance density of the printed dielectric films. We investigated the possibility of decreasing the leakage current by printing double layered dielectric films. It is expected that pin-holes or other possible defects of the first printed layer are filled during the ink deposition of the second layer. Also, there is a possibility that a denser interface lying on a top of more porous material could be formed as noticed for other sol-gel derived multi-layered thin film structures³⁵.

In order to compare the electrical properties of single and double layered capacitor samples C - f , C - V and I - V measurements were made. Both single and double layered samples were fabricated using a printing plate with ink transfer

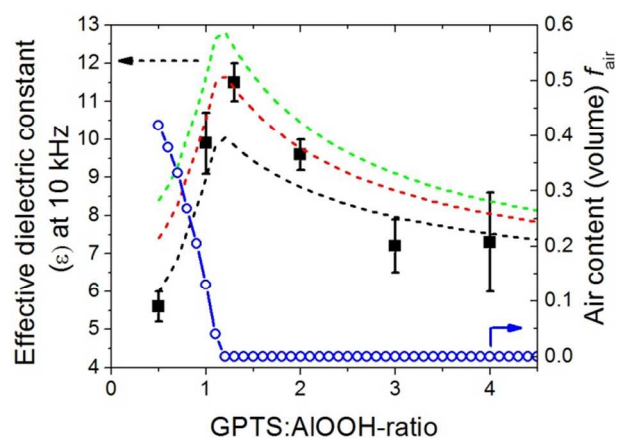


Fig. 11. The measured (black square symbols) dielectric constant (ϵ) of the GPTS:AIOOH films at 10 kHz as a function of increasing GPTS content. The calculated dielectric constant according to the Maxwell-Garnet ternary mixing rule is shown as dashed lines assuming different dielectric constants for AIOOH): black $\epsilon_{\text{AIOOH}} = 20$, red $\epsilon_{\text{AIOOH}} = 30$, and green $\epsilon_{\text{AIOOH}} = 40$. Also shown is volume fraction of air as a function of increasing AIOOH content (hollow blue circles).

Table 3. Measured film thicknesses and capacitances at 10 kHz for gravure printed GPTS:AIOOH single and double layered films. GPTS:AIOOH ratio used was 2:1 ($r = 2.0$).

Sample	Number of layers	Transfer volume (ml/m ²)	C_p/A (pF/mm ²)	Thickness (nm)
#1	1	5.3	168	450
#2	2	5.3	98	650
#3	1	10.4	104	700
#4	2	10.4	53	1400

capacities of 5.3 ml/m² (raster: 140 lines/cm) and 10.4 ml/m² (80 lines/cm). The measured film capacitances and thicknesses are summarized in Table 3.

Single layered films fabricated with a 10.4 ml/m² (80 lines/cm) printing plate (sample #3) were comparable in thickness with the double layered films produced with the 5.3 ml/m² (raster: 140 lines/cm) (sample #2). The measured capacitances of samples #2 and #3 are also close to each other. To study the nature of the double layer structures and to identify if there is any mixing between the first and the second layer of double layered samples, SEM measurements were applied for edges etched with FIB. The SEM images, shown in Fig. 12, indicate that in the double layered sample two individual layers are formed which have the same thickness and a clear interface. In the higher resolution picture some porosity can be seen. This visual observation supports our earlier discussion about the presence of air in the film. For some samples, the edge was formed with KOH etching. In SEM, the etched edges of some of the samples show delamination of the topmost layer from the first layer. From both the observed clear interface and the observed delamination process we can conclude that the two layers in a double-layer film are separate without interfacial mixing and form a back-to-back double layered structure.

The results from I - V measurement of single and double layered samples are shown in Fig. 13. While the one and double layered samples (#2 and #3 respectively) have approximately the same thickness yield in similar capacitance, the double layered

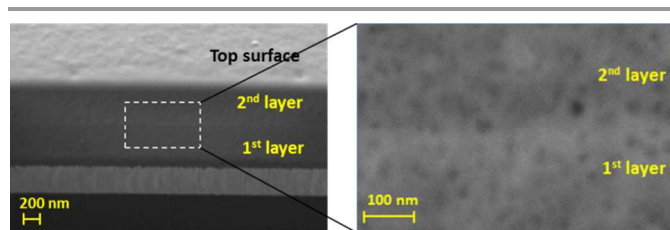


Fig. 12. a) SEM picture taken from an angle on the FIB etched edge of double printed GPTS:AIOOH samples. Substrate, Mo-surface, 1st and 2nd ink layers and the top surface are identified. b) Double magnification showing clear interface between the 1st and 2nd layers.

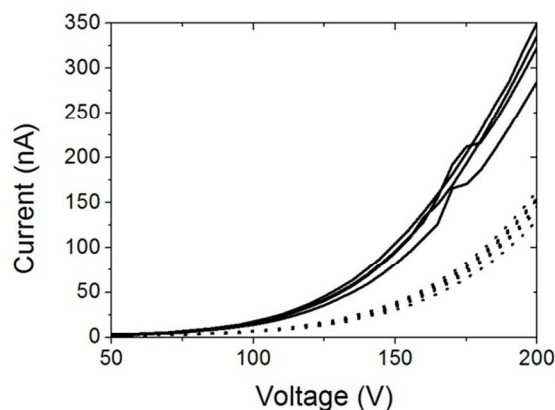


Fig. 13. Results from I - V measurement of single (solid lines) and double (dotted lines) layered samples.

samples have about 50 % lower leakage current than the corresponding single layered samples. Furthermore, the double layered samples have a lower amount of current bursts, probably originating from pinhole burns, than in their single layered analogues. Clearly, the double layered samples can provide higher reliability in comparison to their single layered analogues; thus they are more suitable as dielectric layers for printed electronics applications.

Conclusions

We have successfully synthesized and gravure printed hybrid aluminum oxy-hydroxide (AIOOH) nanoparticle dielectric inks in a GPTS-matrix. Based on printability test, the inks have good printability in tandem with good film formation properties. The fabricated films showed an increasing capacitance density with an increasing AIOOH content until the GPTS:AIOOH w/w ratio of ~1.3. With lower ratios both the capacitance density and the calculated dielectric constant decrease. This behavior could be qualitatively explained by the Maxwell-Garnett ternary mixing rule and the presence of air pores in the film. Such a porous structure of the sol-gel derived nanocomposite affects the electrical properties of the composites with different GPTS:AIOOH ratios. Concurrently, it was found that the leakage current density decreases with increasing GPTS content. The composite with a GPTS:AIOOH ratio of 1.25:1 yielded a capacitance density of 109 ± 2 pF/mm² at 10 kHz frequency and a leakage current density of 60 ± 20 μ A/cm² when using a 0.5MV/cm electric field. The calculated relative dielectric constant at 10 kHz frequency for this composition was 11.2 ± 0.5 , where the error arises both from variation in film thickness and capacitor geometrical dimensions. Double layered films were found to lead to lower leakage current and less soft breakdowns in comparison to single layered films having comparable film composition and film thickness. The use of a double-printed layer offers a simple and effective solution for limiting the leakage current in nanocomposite dielectric films.

Acknowledgements

The research has been supported by the EU FP7 Programme in the Points project (Grant Agreement no. 263042). This work was partially funded by the Portuguese Science Foundation (FCT-MEC) through projects EXCL/CTM-NAN/0201/2012 and PEst-C/CTM/LA0025/2013-14. Daniela Nunes from CENIMAT/I3N is acknowledged for SEM/FIB analysis Professor Isabel M Fonseca and Nuno Costa from REQUIMTE, FCT-UNL are acknowledged for BET analysis. Dr. Neil Graddage, Mrs Elina Jansson, Mrs. Johanna Hiitola-Keinanen, Mr. Olli Heikura and Mr Olli-Heikki Huttunen are also greatly acknowledged for their help.

Appendix

The volume fraction f of the total volume occupied by the inclusions can be expressed as a function of the GPTS:AIOOH weight ratio r as

$$r = \frac{m_e}{m_i}; f = \frac{V_i}{V_i + V_e}; f_w = \frac{m_i}{m_i + m_e}; m = \rho \cdot V \rightarrow f = \frac{\rho_e}{\rho_e + r\rho_i} \quad (\text{A1})$$

where m_i , V_i and m_e , V_e are the masses and volume of the inclusions (AIOOH) and the environment (GPTS), respectively, f_w the fraction of the total mass due to the inclusions and ρ_i and ρ_e the densities of the inclusions and the environment, respectively.

With the help of equation (A1), the pure composite density ρ_c , which includes only GPTS and AIOOH, can be calculated from

$$\rho_c = \frac{(1+r)\rho_e\rho_i}{\rho_e + r\rho_i} \quad (\text{A2})$$

For example, this yields $\rho_c = 2.2$ g/cm³ for the composite with $r = 0.5$. The total volume fraction of air f_{air} can then be estimated when assuming that air present in the pores of the film increases the total volume by using:

$$f_{\text{air}} = \frac{V_{\text{air}}}{V_{\text{air}} + V_c} = \frac{V_{\text{air}}}{V_{\text{air}} + \frac{m_c}{\rho_c}} \quad (\text{A3})$$

which gives $f_{\text{air}} = 0.42$ for 1 g of composite ($m_c = 1$ g). The modified volume fraction of the inclusions is then

$$f_i = 1 - f_{\text{air}} - f_e = 1 - f_{\text{air}} - \frac{V_e}{V} = 1 - f_{\text{air}} - \frac{\frac{m_e}{\delta_e}}{\frac{m_i}{\delta_i} + \frac{m_e}{\delta_e} + V_{\text{air}}} = 1 - f_{\text{air}} - \frac{\left(\frac{r}{r+1}\right)\frac{m_c}{\delta_e}}{\left(\frac{1}{r+1}\right)\frac{m_c}{\delta_i} + \left(\frac{r}{r+1}\right)\frac{m_c}{\delta_e} + V_{\text{air}}} \quad (\text{A4})$$

where the last step arises from the fact that the added air doesn't change the weight ratio f_w shown in equation (A1).

Based on the measured pore volume for the film with $r = 0.5$ and the linearly decreasing projected surface area with increasing GPTS:AIOOH ratio, we have estimated the pore volume V_{air} as linearly decreasing with values shown in Table A1 for $0.5 \leq r \leq 1.1$ and as $V_{\text{air}} = 0$ for $r > 1.1$.

By first calculating ρ_c using equation (A2) followed by obtaining f_{air} using equation (A3), we can finally get f_i using equation (A4). All the parameter values are shown in Table A1

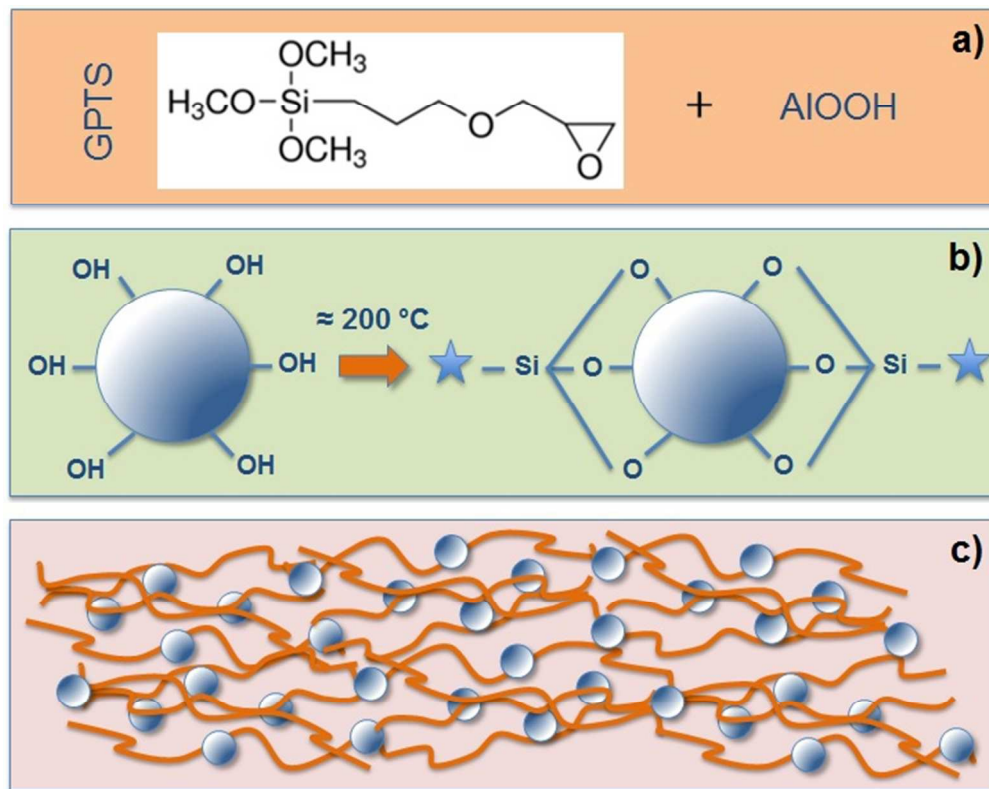
Table A1 Estimated values for air volume V_{air} , calculated values for composite density ρ_c , air volume fraction f_{air} and inclusions volume fraction f_i within GPTS:AIOOH weight ratio of $0.5 \leq r \leq 1.1$.

r	V_{air} (cm ³)	ρ_c (cm ³)	f_{air}	f_i
0.5	0.33	2.190	0.420	0.369
0.6	0.28	2.178	0.379	0.368
0.7	0.23	2.166	0.333	0.370
0.8	0.17	2.156	0.268	0.381
0.9	0.12	2.147	0.205	0.391
1.0	0.07	2.140	0.130	0.404
1.1	0.02	2.132	0.041	0.423

Notably, with the presented assumptions, the ternary model simplifies to the binary model with $r > 1.1$.

References

- (a) K. Sukanuma, in *Introduction to Printed Electronics*, SpringerBriefs in Electrical and Computer Engineering 2014, vol. 74, pp. 23-48.
- (b) M. Jung, J. Kim, J. Noh, N. Lim, C. Lim, G. Lee, J. Kim, H. Kang, K. Jung, A. D. Leonard, J. M. Tour, G. Cho, *IEEE Trans. Electr. Dev.*, 2010, **57**, 571-580.
- (c) A.C. Huebler, F. Doetz, H. Kempa, H.E. Katz, M. Bartzsch, N. Brandt, I. Hennig, U. Fuegmann, S. Vaidyanathan, J. Granstrom, S. Liu, A. Sydorenko, T. Zillger, G. Schmidt, K. Preissler, E. Reichmanis, P. Eckerle, F. Richter, T. Fischer, U. Hahn *Org. Electron*, **8**, 2007, 480-486.
- (d) M. Hamsch, K. Reuter, M. Stanel, G. Schmidt, H. Kempa, U. Fügmann, U. Hahn, A. C. Hübler, *Mat. Sci. Eng. B*, 2010, **170**, 93-98,
- (e) J. Jo, J.-S. Yu, T.-M. Lee, D.-S. Kim, *Jpn. J. of Appl. Phys.* 2009, **48**, 04C181.
- (f) Torbjörk, N. J. Kaihovirta, T. Mäkelä, F. S. Petterson, R. Österbacka, *Org. Electron*. 2008, **9**, 931-935.
- (g) M. M. Voigt, A. Guite, D.-Y. Chung, R. U. A. Khan, A. J. Campbell, D. D. C. Bradley, F. Meng, J. H. G. Steinke, S. Tierney, I. McCulloch, H. Penxten, L. Lutsen, O. Douhert, J. Manca, U. Brokmann, K. Sönnichen, D. Hülseberg, W. Bock, C. Barron, N. Blanckaert, S. Springer, J. Grupp, A. Mosley, *Adv. Funct. Mater.* 2010, **20**, 239-246.
- J. Noh, M. Jung, K. Jung, G. Lee, J. Kim, S. Lim, D. Kim, Y. Choi, Y. Kim, V. Subramanian and G. Cho, *IEEE Electr. Dev. Lett.*, 2011, **32**, 638-640
- M. Jung, J. Kim, J. Noh, N. Lim, C. Lim, G. Lee, J. Kim, H. Kang, K. Jung, A. D. Leonard, J. M. Tour and G. Cho, *IEEE Trans. Electr. Dev.*, 2010, **57**, 571-580
- J. Jo, J.-S. Yu, T.-M. Lee and D.-S. Kim, *Jpn. J. Appl. Phys.* 2009, **48**, 04C181
- R. Sondergaard, M. Hösel, D. Angmo, T. T. Larsen-Olsen and F. C. Krebs, *Mat. Today*, 2012, **15**, 36-49
- J. Hast, M. Tuomikoski, R. Suhonen, K.-L. Väisänen, M. Välimäki, T. Maaninen, P. Apilo, A. Alastalo and A. Maaninen, *SID Symposium Digest of Technical Papers*, 2013, **44**, 192-195
- M. Allen, C. Lee, B. Ahn, T. Kololuoma, K. Shin and S. Ko, *Microelectr. Eng.*, 2011, **88**, 3293-3299
- H. Klauk, *Chem. Soc. Rev.* 2010, **39**, 2643-2666
- H. Minemawari, T. Yamada, H. Matsui, J. Tsutsumi, S. Haas, R. Chiba, R. Kumai and T. Hasegawa, *Nature* 2011, **475**, 364-367
- S. Jeong and J. Moon, *J. Mater. Chem.* 2012, **22**, 1244-1250
- A. Facchetti, M.-H. Yoon and T. J. Marks, *Adv. Mater.*, 2005, **17**, 1705-1725.
- R. P. Ortiz, A. Facchetti and T.J. Marks, *Chem. Rev.*, 2010, **110**, 205-239.
- T. Lehnert, J. Adam and M. Veith, Proceedings of LOPE-C 2011, Frankfurt, 2011.
- F.-C. Chen, C.-W. Chu, J. He, Y. Yang and Jen-Lien Lin, *Appl. Lett.*, 2004, **85**, 3295.
- W.-H. Lee, C. C. Wang and J. C. Ho, *Thin Solid Films*, 2009, **517**, 5305-5310.
- F.-C. Chen, C.-S. Chuang, Y.-S. Lin, L.-J. Kung, T.-H. Chen and H.-P. D. Shieh, *Org. Electron*. 2006, **7**, 435-439.
- L.-H. Chen, P. Lin, J.-C. Ho, C.-C. Lee, C. Kim and M.-C. Chen, *Synth. Met.*, 2011, **161**, 1527-1531.
- H. Y. Noh, Y. G. Seol, S. I. Kim and N.E. Lee, *Electrochem. Solid-State Lett.* 2008, **11**, H218.
- R. Schroeder, L. A. Majewski and Martin Grell, "Adv. Mater. 2005, **17**, 1525-1539.
- A. Rasul, J. Zhang, D. Gamota and C. Takoudis, *Microel. Eng.*, 2012, **93** 95-99.
- X. Wu, F. Fei, Z. Chen, W. Su and Z. Cui, *Comp. Sci. and Tech.*, 2014, **94**, 117-122.
- (a) R. Kasemann, H. Schmidt and E. Wintrich, In *Better Ceramics Through Chemistry VI*, ed. A. K. Cheetham, C. J., Brinker, M. L., McCartney and C. Sanchez, Materials Research Society, San Francisco, 1994. pp. 915-921.
- (b) H. Schmidt, P. W. Oliveira and S. Sepeur, in *Ceramics: Getting into the 2000's - Part C*, ed. P. Vincenzini, Faenza, 1999. pp. 451-465.
- (c) S. Sepeur, N. Kunze, B. Werner and H. Schmidt, *Thin Solid Films*, 1999, **351**, 216-219.
- J. Mauricio, L. A. Rocha, F. A. Sigoli, Y. Messaddeq, J. Dexpert-Ghys and S. J. L. Ribeiro, *J. Non-Cryst. Solids*, 2008, **354**, 4795-4799.
- J. H. Jun, H. J. Kim and D. J. Choi, *J. Ceram. Proc. Res.*, 2008, **9**, 75-78
- C. Avis and J. Jang, *J. Mat. Chem*, 2011, **21**, 10649-10652.
- J. B. Kim, D. R. Kwon, K. Chakrabarti, C. Lee, K.Y. Oh and J. H. Lee, *J. Appl. Phys.* 2002, **92**, 6739-6742.
- R. Tettenhorst and D. A. Hofmann, *Clays and Clay Minerals*, 1980, 373-380.
- P. Alphonse and M. Courty, *ThermoChim.Acta*, 2005, **425**, pp. 75-89.
- T. Kololuoma, J. Leppaniemi and A. Alastalo, Proceedings of the Lope-C 2012, Munich, 2012.
- K. Vishista and F. D. Gnanam, *Mat. Lett.*, 2004, **58**, 1576-1581.
- W.-H. Lee, C.-T. Liu and Y.-C. Lee, *Jpn. J. Appl. Phys.* 2012, **51** 061603
- A. Sihvola, in *IEE Electromagnetic Series 47*, The Institution of Electrical Engineers, London, 1999.
- A. Maliakal, H. Katz, P.M. Cotts, S. Supramoney and P. Mirau, *J. Am. Chem. Soc.*, 2005, **127**, 14655-14662.
- C.J. Brinker, and G. W. Scherer, In *Sol-gel Science: The Physics and Chemistry of Sol-Gel Processing*, Academic Press Inc., San Diego, 1990.
- M. A. Aegerter, A. Reich, D. Ganz, G. Gasparro, J. Pütz and T. Krajewski, *J. Non-Cryst. Solids*, 1997, **218**, 123-128.



191x152mm (96 x 96 DPI)